

Laboratory simulation of impacts on aluminum foils of the Stardust spacecraft: Calibration of dust particle size from comet Wild-2

A. T. KEARSLEY^{1*}, M. J. BURCHELL², F. HÖRZ³, M. J. COLE², and C. S. SCHWANDT³

¹Impact and Astromaterials Research Centre, Department of Mineralogy, The Natural History Museum, London SW7 5BD, UK

²Centre for Astrophysics and Planetary Sciences, School of Physical Science, University of Kent, Canterbury, Kent CT2 7NH, UK

³NASA Johnson Space Center, Houston, Texas 77058, USA

*Corresponding author. E-mail: antk@nhm.ac.uk

(Received 02 November 2005; revision accepted 07 January 2006)

Abstract—Metallic aluminum alloy foils exposed on the forward, comet-facing surface of the aerogel tray on the Stardust spacecraft are likely to have been impacted by the same cometary particle population as the dedicated impact sensors and the aerogel collector. The ability of soft aluminum alloy to record hypervelocity impacts as bowl-shaped craters offers an opportunistic substrate for recognition of impacts by particles of a potentially wide size range. In contrast to impact surveys conducted on samples from low Earth orbit, the simple encounter geometry for Stardust and Wild-2, with a known and constant spacecraft-particle relative velocity and effective surface-perpendicular impact trajectories, permits closely comparable simulation in laboratory experiments. For a detailed calibration program, we have selected a suite of spherical glass projectiles of uniform density and hardness characteristics, with well-documented particle size range from 10 μm to nearly 100 μm . Light gas gun buckshot firings of these particles at approximately 6 km s^{-1} onto samples of the same foil as employed on Stardust have yielded large numbers of craters. Scanning electron microscopy of both projectiles and impact features has allowed construction of a calibration plot, showing a linear relationship between impacting particle size and impact crater diameter. The close match between our experimental conditions and the Stardust mission encounter parameters should provide another opportunity to measure particle size distributions and fluxes close to the nucleus of Wild-2, independent of the active impact detector instruments aboard the Stardust spacecraft.

INTRODUCTION

The Stardust mission has a primary objective to collect cometary dust particles from comet Wild-2, and return them to Earth (Brownlee et al. 2003). The timeline, geometry, and velocity for the encounter with Wild-2 are described by Brownlee et al. 2003 and the aerogel collection system is described by Tsou et al. 2003. Real-time sensors aboard the spacecraft detected a large number of particle impacts during the 264 sec before and 922 sec after the closest approach to the comet nucleus (Tuzzolino et al. 2004). Data from the bumper shield impact detection sensors suggests that 2800 ± 500 particles with sizes greater than 15 μm have been implanted within exposed silica aerogel blocks (Tuzzolino et al. 2004), which will form the main focus of post-flight investigation. However, it should be noted that the two real-time detection systems on board the spacecraft returned impact data (Kissel et al. 2003; Tuzzolino et al. 2004) with different sensitivities in terms of momentum threshold (i.e.,

the range of mass and velocity product), and there are apparent discrepancies between their impact count rates (Tsou et al. 2004). The impact ionization system (Kissel et al. 2003) indicated a significantly lower flux than the more widely reported bumper shield data. Laboratory experiments utilizing monomineralic and powdered meteorite projectiles with a diameter greater than 20 μm have shown that remnants of these grains can be recognized in impact tracks within aerogel, although there is often evidence of fragmentation during emplacement (Graham et al. 2005), making determination of original particle size very difficult. The potential extent of this problem is shown by observations of aerogel exposed on the Mir station, where the measured size of projectile residue had no systematic relationship with the size of penetration tracks (Hörz et al. 2000). It has not yet been convincingly demonstrated that much smaller silicate particles (e.g., 1 μm in diameter) will leave recognizable traces in aerogel. Evidence from interplanetary dust detectors (e.g., Grün et al. 1992, 1995) and from spacecraft materials

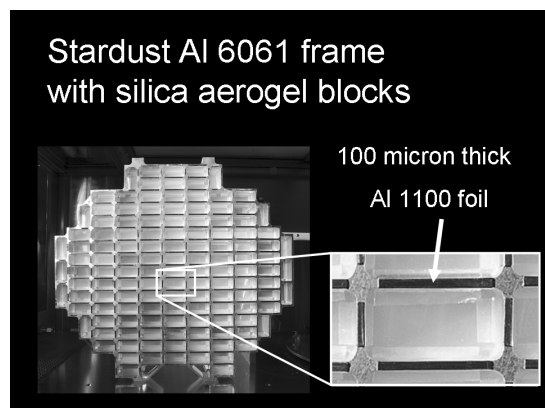


Fig. 1. The Stardust aerogel collector aluminum frame with an enlarged detail of four foil sheets (reflective, appearing dark) around an aerogel block. (Image courtesy of NASA/Caltech/JPL)

returned from low-Earth orbit (LEO) (e.g., Moussi et al. 2005) suggests that there are abundant micrometeoroids of micron scale, although the relative contribution from asteroid and comet sources has not yet been firmly established. Although not widely realized, another component of the Stardust spacecraft may yield valuable information as to the size distribution of particles encountered. In addition to the 1039 cm² area of aerogel on the comet collection face, 153 cm² of aluminum foil (Fig. 1) was also exposed to impact (Tsou et al. 2003). It is likely that these foils have preserved a record of impacts from sub-micron scale upwards.

Many spacecraft surfaces exposed to space in LEO have been examined for signs of impact damage (e.g., Warren et al. 1989; Humes 1991; See et al. 1994; Zolensky et al. 1994; Love et al. 1995; Bernhard and Hörz 1995; Graham et al. 2001; Moussi et al. 2005). Metal surfaces present a relatively hard and dense substrate and may therefore result in high levels of modification to the impacting particle (Bernhard et al. 1994a; Graham et al. 2001) during the creation of a distinctive bowl-shaped crater. Aluminum alloys are the metals employed most extensively (Dunn 1997), usually containing Mg, Mn, Fe, and Cu in concentrations of a few parts per thousand to a few percent (Davis 1998), often segregated heterogeneously on a scale of microns (e.g., Fig. 4). Successful laboratory simulation of hypervelocity impact features on aluminum foils was reported by Hörz et al. (1993). Where recognition of particle origins is an important goal for an impact survey (e.g., Kearsley et al. 2005), confusion of the substrate composition with that of impacting space debris may be a problem, unless a substantial amount of residue is present (Graham et al. 2004). Fortunately, micrometeoroid remains are easily recognized on aluminum surfaces, where their distinctive mafic silicate and sulfide residues stand out (Bernhard et al. 1994a, 1994b; Brownlee et al. 1994). For surfaces that have been returned from LEO, difficulties attend the interpretation of the mass of individual

impacting particles due to unconstrained variables, i.e., the crater characteristics reflect their mass and velocity, both unknown quantities that have no simple and unambiguous individual proxies. Surveys of spacecraft impact damage (e.g., Moussi et al. 2005) derive flux models detailing numbers of specific particle size, but need to rely upon assumptions of a mean velocity as well as density for micrometeoroids, which cannot fully reflect the diverse range of natural particle populations. The apparently circular outline of most impact craters may also poorly reflect the diversity of incidence angles and therefore can mask a range of effective impact velocities. Most laboratory simulations of impacts upon ductile substrates have employed a target-perpendicular shot trajectory and relatively well-constrained particle diameters, hardness, density, mass, and velocity. Relatively few experiments (e.g., Christiansen et al. 1993; Burchell and MacKay 1998) have looked at oblique incidence impacts or impacts from notably non-spherical projectiles. There are thus difficulties in making direct comparison between laboratory experiments and the complex situation in LEO (Love et al. 1995). In addition, although many LEO impact features do record micrometeoroid impacts (for example, 45 craters with micrometeoroid residues, 38 with space debris residues and 28 with no recognizable residue reported in a survey of 111 impact features on the Hubble Space Telescope by Kearsley et al. 2005), it is not possible to distinguish cometary, asteroidal, and interstellar origins.

In the case of the Stardust encounter, the on-board impact sensors have demonstrated that the vast majority of the impacting particle collection on the front face of the spacecraft was acquired during the few minutes around the closest approach to the nucleus of comet Wild-2 (Tuzzolino et al. 2004), with 2300 ± 400 particles with a diameter greater than 15 μm captured by the aerogel. Later bursts of activity, mostly from smaller particles, were also recorded some 620–720 seconds after the closest encounter, with perhaps 500 ± 200 particles with a diameter greater than 15 μm being captured in the aerogel. Together these collections may thus be taken as a true reflection of a cometary source. The dominant component of the relative impacting velocity particle is believed to be that of the spacecraft relative to the nucleus (6.1 km/s^{-1}), resulting in impacts at a known velocity at near surface-perpendicular incidence. Thus the important attributes of the Stardust mission particle to foil encounter fall neatly within the capabilities of laboratory experiments.

In addition to documenting the relationship between particle size and the diameter of the resulting crater, we have also investigated effects of particle composition, density, and hardness for a range of known projectile materials. The role of such particle properties in influencing crater morphology and their recognition from impact residues is to be reported in a future paper. In this paper, we concentrate on determining the impacting particle diameter from the size of impact feature.

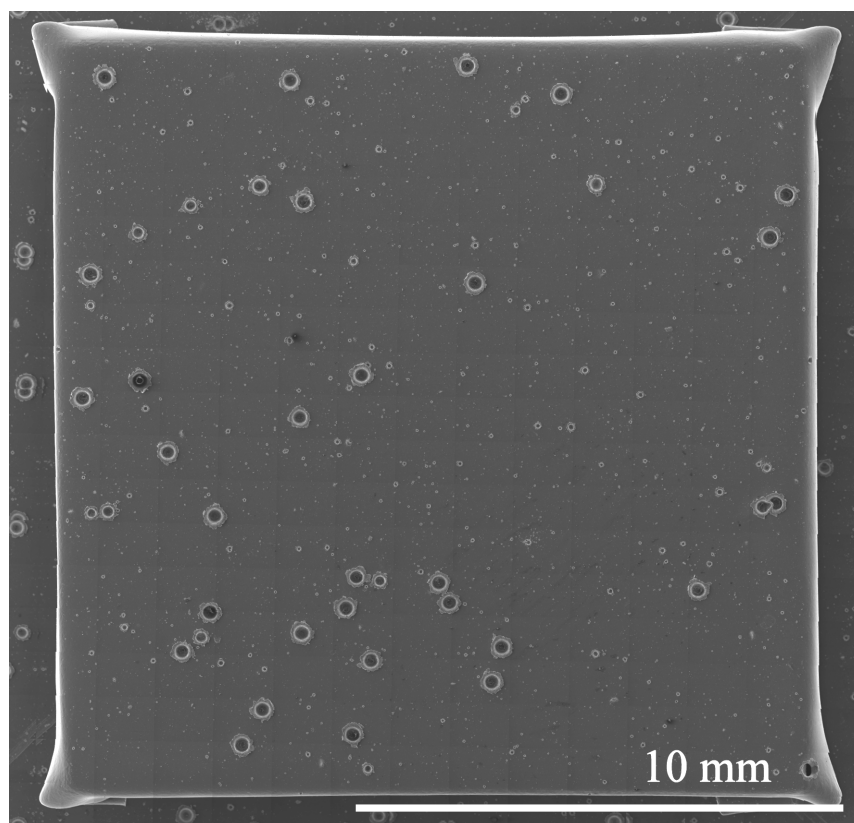


Fig. 2. Montage of secondary electron images showing numerous impacts by soda-lime glass spheres of 62 μm in diameter.

IMAGERY AND MEASUREMENT OF PROJECTILE AND IMPACT FEATURE DIMENSIONS

Previous studies of impacts on space-exposed surfaces (e.g., Love et al. 1995) have used a calibrated mechanical stage and shallow-focus-field compound optical microscopy for rapid determination of the crater internal diameter at the original surface level, with a precision of about 2 μm (Brownlee, personal communication). For this study, we chose scanning electron microscopy (SEM) rather than optical methods, as the higher resolution permits better precision in the measurement of the very small craters (less than 5 μm in diameter), which may be very numerous on the Stardust foils. Unfortunately, the excellent lateral spatial resolution of SEM is also accompanied by substantial depth of focus, usually considered a desirable feature, but which prevents easy and reproducible recognition of the precise line of intersection between the crater inner slope and the ambient plane of the original uncratered surface in individual SEM images. Although the inner crater diameter can be reliably located by use of stereometric software, the process is very time consuming for large numbers of craters. We concluded that reported measurements should be based upon a simple morphological feature, the crater lip top diameter (Fig. 10), easily recognizable in all SEM models, wherever used. However, we also present a calibration line based upon

optical microscope measurement of the crater internal diameter in the same foils, for comparison with previous studies (Fig. 14).

All of the SEM imagery and measurement reported in this paper was performed on a JEOL 5900 LV instrument in the Electron Microscopy and Mineral Analysis division of the Department of Mineralogy at the Natural History Museum, London. All images were taken using 20 kV accelerating voltage at high vacuum, with backscattered electron images (BEI) and secondary electron images (SEI) of magnifications between $\times 100$ and $\times 500$ collected using an Oxford Instruments INCA X-ray energy dispersive microanalyzer, running version 15 software. Entire target foils were documented by automated image montage creation (Fig. 2), with storage of individual image frames for later examination at high resolution and subsequent measurement of features using the digital callipers in the INCA software. Image size calibration was performed by collection of images from features on a Richardson high-magnification test slide (model 80302, serial 10461) at the same magnifications and working distance as were employed for projectile and crater imagery, yielding an excellent linear fit across a wide size range between the published size of features on the calibration slide and the figures derived from the digital calliper measurements (Fig. 3). Error on linear dimension measurements was determined as a standard deviation of less than $\pm 1\%$ in all calibration images.

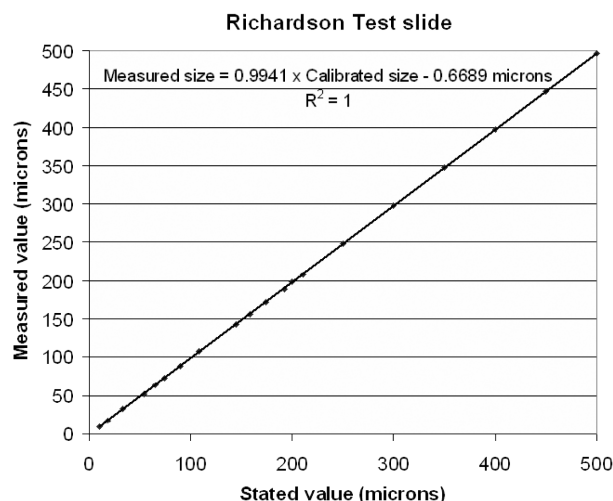


Fig. 3. Plot of SEM digital caliper measurements on Richardson test slide features (y-axis) against certified values (x-axis). Note excellent linear correlation within 1% of certified values.

IMPACT MATERIALS AND TECHNIQUES

The Target

In all shots the targets were samples of the same metal alloy foil as employed on Stardust (100-micron-thick Al 1100). The surface morphology and composition of the foil was examined by backscattered electron images of a small ($\sim 1 \text{ cm}^2$) sub-sample, revealing a relatively smooth surface showing subtle linear surface striations due to the rolling fabrication process for the foil, weak electron channelling contrast delimiting metal domain structure, and bright inclusions of iron-rich phases within the alloy (Fig. 4).

Projectiles

For our extensive shot program, projectiles were selected to evaluate the influence of a range of variables, including size, shape, density, hardness, and chemical composition. The resulting impact craters have been examined to provide information upon the relationship between projectile diameter and crater diameter, deviation from circular shape as a function of projectile shape, the location of projectile residue, the modification of projectile composition, and the recognition of specific minerals likely to occur within cometary dust samples.

However, in this paper we concentrate upon the results from ten shots that utilized projectiles of a single composition (soda-lime glass), and hence similar density and hardness. To minimize dispersion of crater dimensions as a result of complex impactor morphology, we used spherical projectiles of well-constrained size distribution. The shots at Kent and NASA included several examples of the same projectile size for consistency checks between laboratories and several

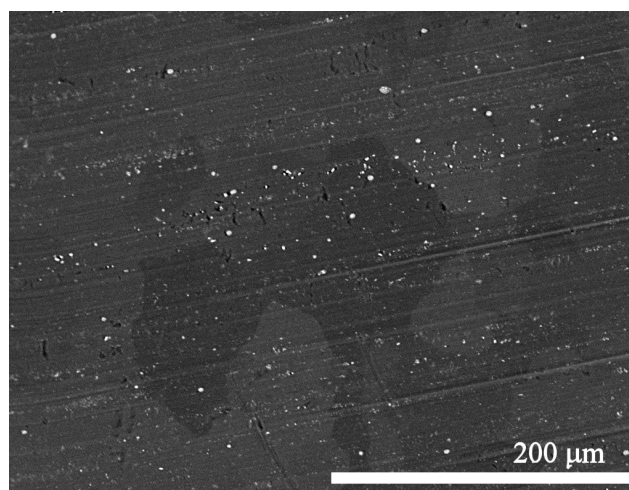


Fig. 4. Backscattered electron image of a piece of the Stardust Al 1100 foil, showing linear surface striations, channelling contrast from discrete metal grains (variations in background grey tone), and iron-rich alloy inclusions (bright areas).

distinct sizes to widen the calibration range. The soda-lime glass beads were supplied by White House Scientific (see <http://www.whitehousescientific.com>), sieved to a certified size distribution, with the error bars given in Table 1 corresponding to the ± 1 range about the mean in the size distribution. Optical microscope scan measurements (University of Kent) and SEM images (Natural History Museum, London) of all the bead samples sizes were taken to test their size distribution, for example, Fig. 5. The histograms and statistical analyses of the projectile samples (Fig. 6, with sample sizes given in Table 1) show that most have a tight clustering of size around a single-size mode within 1 of the mean value as supplied by Whitehouse Scientific, but in some cases the distributions had greater dispersion than specified. For example, the smallest sphere sample employed (Fig. 5) had a much broader range of projectile dimensions, with many of sizes down to 50% of the mode dimension. In the larger bead samples, some small grain protrusions were evident ($\sim 10\%$ of beads) and 5% of beads were smaller than expected. There were very few broken beads, although the crater size distribution does suggest that some projectiles did fragment during the violent acceleration to impact velocity. Nevertheless, the measured glass projectiles yielded an easily determined size calibration, with average diameters and standard deviations given in Table 1 and used in the following analysis.

Experimental Shot Program

Light gas gun shots were performed in two separate facilities: at the University of Kent in Canterbury, England (Burchell et al. 1999), and at the Johnson Space Centre of the National Aeronautics and Space Administration (NASA) in Houston, Texas, USA. Both laboratories used similar small caliber two-stage light gas guns with many common features.

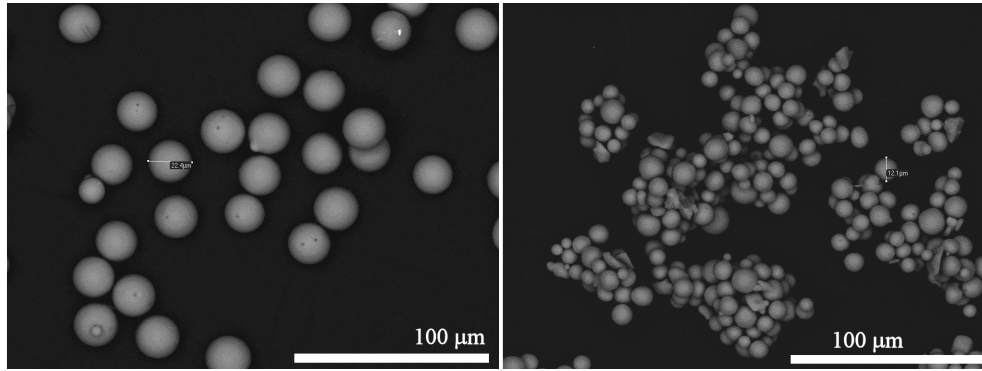


Fig. 5. Backscattered electron images of soda-lime glass bead projectiles showing uniform size in the nominal 22.8-micron sample (left), but broader distribution in the nominal 11.58-micron sample (right). Note digital measurement calipers on images.

Table 1. Light gas gun shots with soda-lime sphere projectiles. A comparison of crater lip diameters and glass bead projectile diameters, all measured by SEM.^a

Soda-lime glass projectiles	Nominal projectile diameter $\pm\sigma$ (μm)	Projectile diameter measured $\pm\sigma$ (μm) Sample (n)	Impact speed (km s^{-1}) $\pm 2\%$	No. of craters on foil	All crater diameters SEM average $\pm\sigma$ (μm) (max./min. avg. and σ)
Kent	11.58 ± 0.19	9.84 ± 2.23 (104)	5.93	51	39.41 ± 8.73 (1.07 ± 0.04)
NASA	11.58 ± 0.19	9.84 ± 2.23 (104)	6.06	44	51.04 ± 9.46 (1.05 ± 0.03)
Kent	22.81 ± 0.78	21.87 ± 0.92 (35)	5.97	62	81.75 ± 23.93 (1.05 ± 0.03)
Kent (free rear)	22.81 ± 0.7	21.87 ± 0.92 (35)	5.92	47 (part)	95.43 ± 10.28 (1.06 ± 0.04)
NASA	22.81 ± 0.78	21.87 ± 0.92 (35)	6.12	38	81.52 ± 27.3 (1.05 ± 0.03)
Kent	35.0 ± 0.8	34.72 ± 1.01 (94)	6.05	32	143.13 ± 26.35 (1.06 ± 0.04)
NASA	35.0 ± 0.8	34.72 ± 1.01 (94)	6.21	101	173.58 ± 38.94 [1.05 ± 0.03]
Kent	42.68 ± 0.55	42.3 ± 1.02 [25]	6.09	91	184.33 ± 26.43 (1.05 ± 0.03)
NASA	49.21 ± 0.72	49.29 ± 3.17 (118)	6.03	93	228.88 ± 30.78 (1.05 ± 0.03)
Kent	63.84 ± 0.8	64.05 ± 2.8 (75)	6.05	74	278.53 ± 30.44 (1.07 ± 0.04)
Kent	83.4 ± 0.8	84.18 ± 2.8 (49)	6.22	38	364.86 ± 45.49 (1.04 ± 0.02)
Kent (free rear)	83.4 ± 2.0	84.18 ± 2.8 (49)	5.96	8	385.71 ± 10.97 (1.03 ± 0.02)
Kent (empty sabot)	n/a	n/a	n/a	14	40.57 ± 16.38

^aCrater diameters are based upon the raw data set, with no threshold for fragmented projectile; n/a (not applicable) refers to the empty sabot shot where there are no known appropriate dimensions for intended projectiles.

The gun barrel bore was 5 mm (NASA) and 4.3 mm (Kent). The guns employed a variety of mechanical apertures, a sabot catcher system and (NASA gun only) flapper valves that minimized the contamination on the target site by fine grained debris from a variety of sources (high-pressure piston, stainless steel burst diaphragm, gun barrel, and sabot catcher). On each gun, independent velocity measurement stations using combinations of laser occultation methods, IR photo diodes, and impact momentum sensors determined the velocity of the sabot pieces; additionally, in the NASA gun, the actual projectile arrival at the target site was monitored by an impact flash detector, i.e., another photo diode. Typically, sabot velocity and projectile velocity agreed to better than 1% (NASA) and 2% (Kent). The intended speed in each shot was 6.1 km s^{-1} , the nominal Stardust encounter speed at comet P/Wild-2. There were slight variations from shot to shot, and the measured speed for each is given in Table 1.

It is not practical with light gas guns to launch individual particles $<250 \text{ }\mu\text{m}$; this is the reason why all projectiles

employed in this paper were “shotgunned” or “buckshot,” i.e., launched as an ensemble of projectiles. Depending on projectile size, some tens to hundreds of individual particles were loaded into a small, central cavity of a four-piece, serrated sabot (both guns used similar sabots). By design, the four sabot quadrants separated radially during free flight, yet allowed a substantial fraction of the projectile ensemble to remain on straight trajectories and to ultimately reach the target site. A number of mechanical apertures assured that only those particles that resided within <1 degree of the gun axis reached the target; all others were terminated by mechanical apertures, including the sabot pieces. During each shot, the target chamber was evacuated to typically a few 10^{-1} mbars or better.

The foil target was held upon a massive aluminum plate. At NASA, Al 6061-T6 was used (the same grade as the Stardust frame on which the foils are mounted in space), some 2.47 cm (1”) on the side and 0.62 cm (1/4”) thick. At Kent Al 6068 was used (Al 6068 is an alloy with similar physical

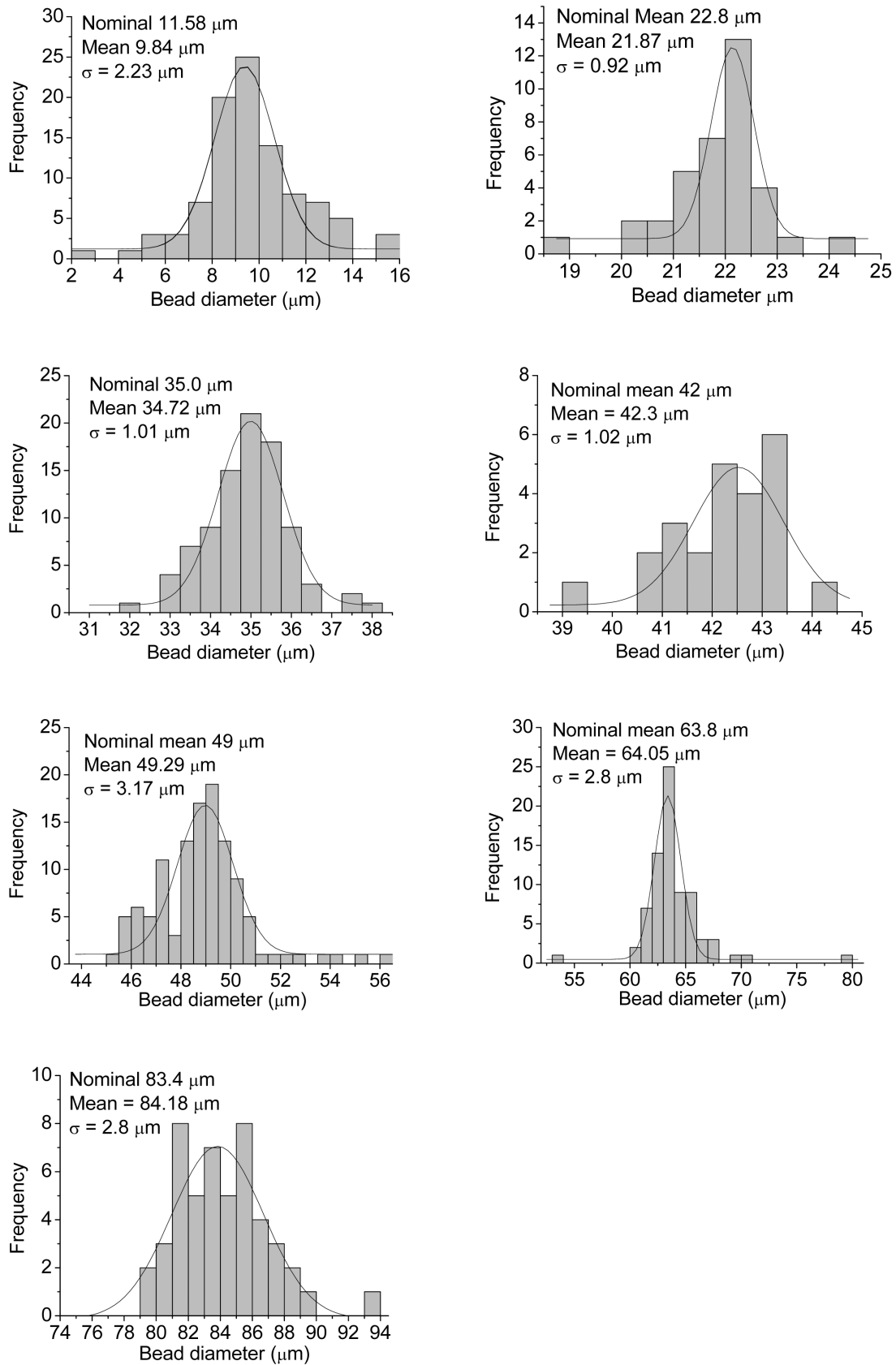


Fig. 6. Particle diameter histograms for the soda-lime glass bead projectiles used for light gas gun shots at NASA and Kent.

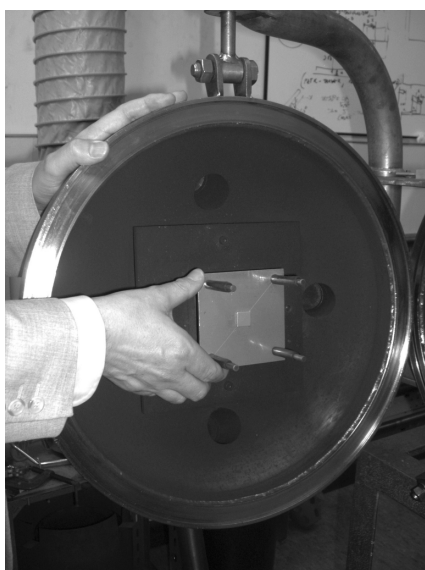


Fig. 7. A foil-wrapped 15 mm plate mounted upon an aluminum base plate (drilled with four locating holes for support) is placed on the target holder in the light gas gun chamber at Kent.

properties to Al 6061) some 1.5×1.5 cm across and 0.2 cm thick. These plates were wrapped as tightly as possible with the thin aluminum foil using pliers. The foil was 100 μm thick (4/1000" nominal), made of aluminum 1100, but of unknown temper grade and annealing history; however, the foil used and kindly supplied by P. Tsou (JPL) was from exactly the same batch that was also used on the Stardust mission. This target arrangement resembled the basic Stardust instrument configuration and materials to permit high-fidelity comparative experiments. Once wrapped, targets were placed in the gun. For example, at Kent they were secured to a larger aluminum (HE30) plate (10×10 cm) for mounting in the gun, as shown in Fig. 7. Two shots were also performed at Kent on the Al 1100 foil suspended with a free rear surface to test the influence of the mounting on crater size and foil penetration. In addition, an extra control shot was done (at Kent), which used the same target as normal, but no projectiles were loaded in the sabot. This provided a target surface that had been exposed to the gun environment during a shot and that could be used as a baseline reference for determination of gun artifacts.

IMPACT FEATURES AND THEIR MEASUREMENT

To ensure comparability of data sets between laboratories that will participate in the Stardust foils analysis, and by common agreement among those that constitute the Stardust Preliminary Investigation Team, it was decided that impact feature measurements should be based on the crater diameter as defined by intersection with a projected horizontal surface laid upon the raised crater lip (Fig. 8). This measured dimension is equivalent to the crater diameter (D) as

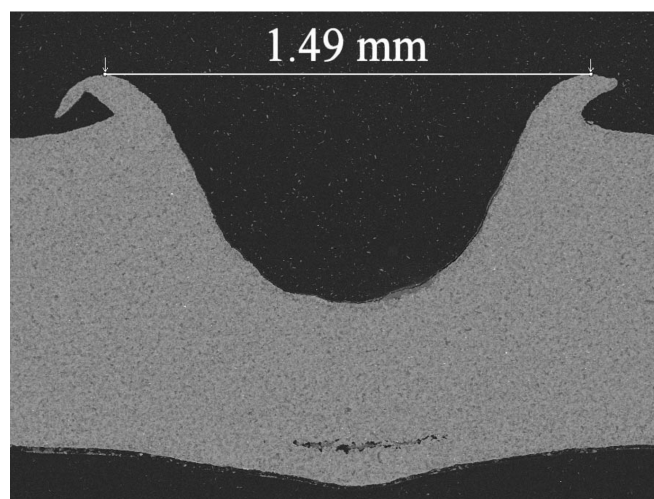


Fig. 8. A backscattered electron image of a vertical section through an impact crater on aluminum. Crater diameter is defined as length of the horizontal line indicated.

employed in studies of impacts on the Long Duration Exposure Facility by e.g., See et al. (1994). High-precision measurements of the crater inner diameter and the crater depth relative to the level of the ambient metal surface can be performed by stereometry of multiple SEM images with known angular separation, although the process is very laborious for a large number of craters on an extensive flat surface, even with modern processing routines. Similarly, the shallow depth of focus of most optical microscopes allows relatively easy measurement of the crater internal diameter at the ambient plane, but has a lower spatial resolution than SEM techniques. However, the narrow dispersion of crater diameter to depth ratios seen in micrometeoroid impact craters on LDEF (Love et al. 1995) and the relatively modest control of crater morphology by projectile density at $>6 \text{ km s}^{-1}$ (Humes 1991), suggests that the size of a single crater feature such as D may suffice for determination of particle size, especially if there is a narrow range of impact velocities, as in the case of the Stardust encounter. Nevertheless, there is evidence that different particle compositions may yield different impact penetration depths (Wallis et al. 2002), and as part of our continuing research we are investigating the role of specific particle characteristics in controlling crater morphology.

Secondary electron images (SEI) taken perpendicular to the foil surface show complex textures on the crater lip, and it can be difficult to recognize the proper point at which to draw the end of the measurement callipers. On some craters, it may be easier to locate appropriate points for measurement by use of backscattered electron imagery (BEI). The geometric position of the solid-state BE detector in the JEOL 5900 sample chamber (an annular ring around the lower aperture of the objective lens) results in a maximum signal level from surfaces that are perpendicular to the electron beam incidence. This detector location intersects the path of

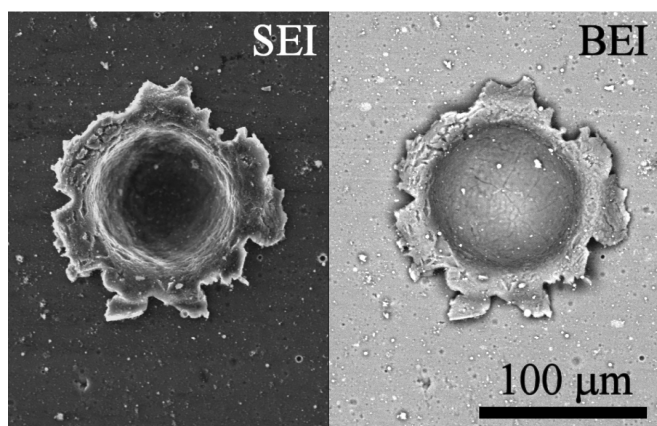


Fig. 9. A comparison of secondary electron (left) and backscattered electron images (right) showing topographic contrast used to define horizontal surface of crater lip.

numerous, high energy electrons that have undergone high angle scattering from the dense metal. Surfaces that are inclined to the electron beam (such as the crater interior wall and the inclined margins of the crater lip) will appear darker in BEI due a greater proportion of the energetic beam electrons being scattered at an angle away from the small, localized detector (Fig. 9). It is, therefore, relatively easy to locate the mid point between the outer lip slope and the crater pit wall in BEI and to utilize this location as the standard measurement point.

For this calibration study, three measurements were taken from each crater that possessed an intact, continuous uplifted oval to circular rim, with an angular spacing of approximately 60 degrees (Fig. 10). Overlapped impact features (uncommon on most targets) were not included in the data set as their dimensions may reflect interference between crater-forming events on a damaged substrate. On features with incomplete rims, two or occasionally only one measurement could be taken. The average diameter value for each crater was tabulated and is plotted in the bins shown on the histograms of Figs. 11 and 12.

Results from Projectile and Impact Feature Size Measurement

We have omitted the very smallest craters (of less than 15 μm and therefore less than twice the peak minimum glass bead diameter) from the statistics as they appear on target foils throughout the shots, including the blank sabot shot, and we believe them to represent fine gun debris and fragmented projectiles.

Two notable features stand out in each of the histograms in Fig. 11: 1) concentration of crater dimensions into a peak between four and five times the projectile diameter; and 2) a substantial “tail” of smaller craters. The projectile size range determined by calibrated SEM imagery of each glass sphere sample does show some dispersion around the nominal size

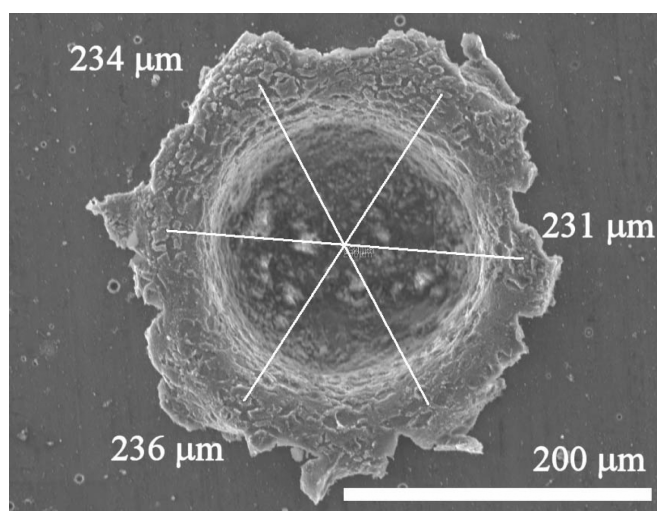


Fig. 10. A secondary electron image of a crater produced by impact of a pyroxene enstatite grain on Stardust foil. The lines of three diameter measurements by digital callipers are shown.

peak (Fig. 6), especially in the smallest particles, but insufficient to account for the “tail” on the lower size shoulder of the crater size mode. Our in-situ measurements of projectile velocity show little dispersion ($\pm 2\%$) within a shot and we attribute these smaller craters to impacts by fragmented projectiles. On the Stardust foils, of substantially greater thickness than the diameter of our projectiles, there seems to be relatively little influence of subtle differences in particle shape on crater circularity. There is no correlation between abundance of smaller craters and irregular shape, hence the small variation in crater maximum/minimum diameters, shown in the final column of Table 1. Our preliminary results from a survey of impacts by markedly inequant pyroxene grains with a high shape factor (i.e., a rod or plate morphology) onto Stardust foils does not show a greater range of crater outline shape than seen in the glass bead shots and we therefore regard crater shape on such foils as relatively insensitive to projectile form. However, impacts onto much thinner foils may preserve a closer proxy to the projectile size and shape as the particles pass through the full foil thickness, and we intend to perform this experiment to verify projectile fragmentation. Shots of the same projectiles into aerogel targets do show evidence of some particle fragmentation but whether during acceleration and flight to the target or on impact is unknown. In conclusion, although the impact craters may reflect the particle size distribution encountering the target, they probably do not give a perfect representation of the particle size distribution in the sabot before firing.

This artifact of the extremely high acceleration in light gas gun shots will not be a factor in the creation of cometary particle impacts on the Stardust spacecraft, where dimensions are expected to be a simpler reflection of the impacting particle size distribution. However, for a suite of calibration

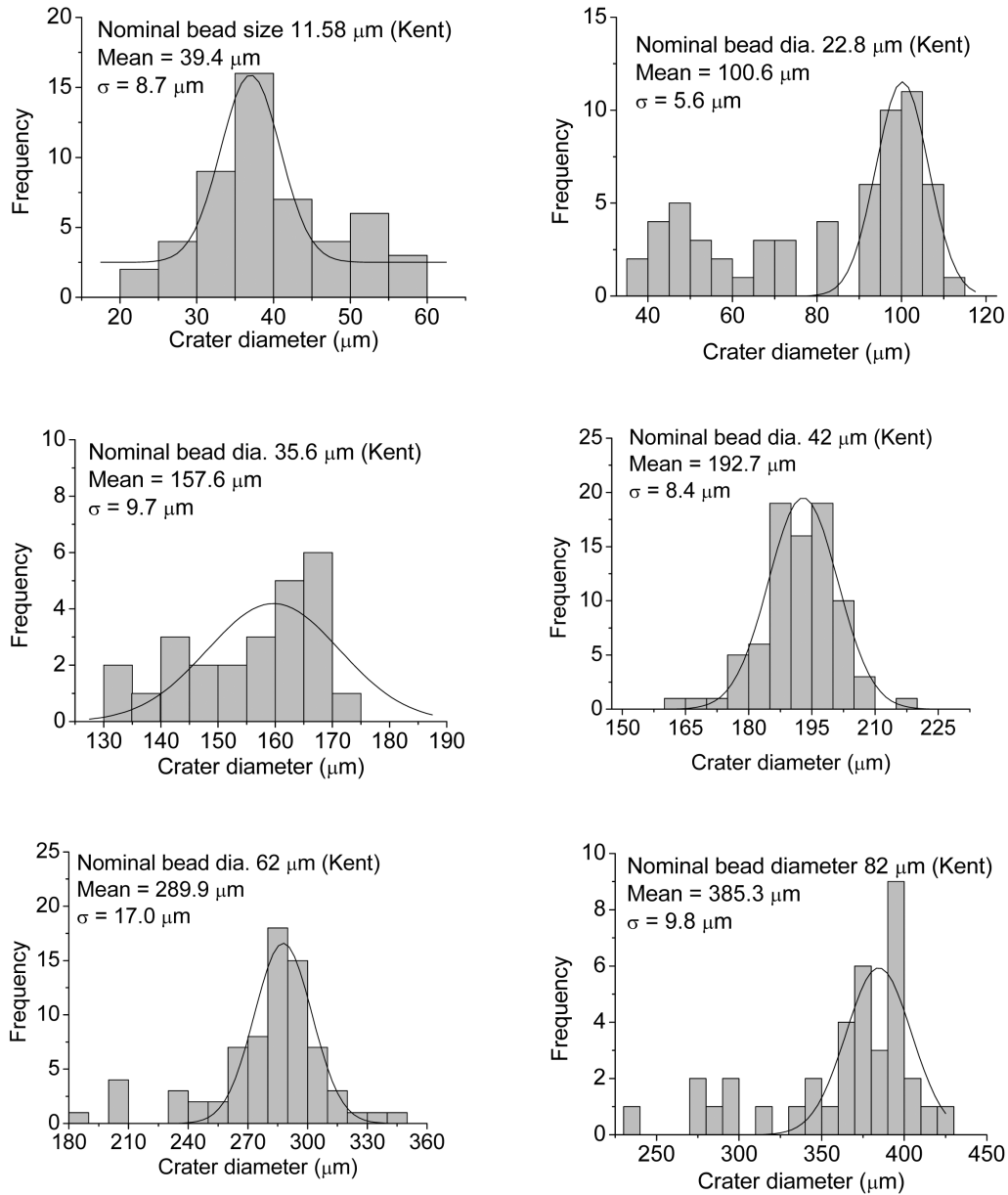


Fig. 11. Histograms of impact crater diameters for each wrapped foil shot at Kent.

experiments, it is necessary to exclude data from projectile fragments of unknown size. We present the raw size data in Table 1 and statistics for crater diameters above a minimum threshold value of 4 times the projectile modal diameter (superimposed graphs and data in Figs. 11 and 12) as the lower limit for inclusion within the sample plotted on the calibration graph for the metal-wrapped foil shots (Fig. 13). Filtering of the data set by this threshold leads not only to an inevitable reduction in standard deviation, but also a marked improvement in the quality of linear regression fit to a straight line. For almost all the crater size distributions, the exclusion of data from less than 4 times the projectile size does not impinge upon the mode seen in the histograms, except for the smallest projectile sample where this cutoff point is within the

substantial small-size shoulder of the mode, reflecting the wide range of sizes in this projectile sample. In the analysis, we therefore do not apply this cut on the data for the impact craters from the smallest projectile sample. However, it is notable that following imposition of the 4 times diameter filter, all of the point plots from twelve shots, including shots from both NASA and Kent laboratories, fall within one standard deviation of the linear fit. There is thus demonstrable linear proportionality between projectile diameter and resulting crater diameter. As particle mass should be proportional to the cube of the projectile radius, this gives a mass dependent exponent of 0.333, close to the 0.352 determined experimentally by Humes (1991). Variation in impact velocity between shots (from 5.85 km s^{-1} to

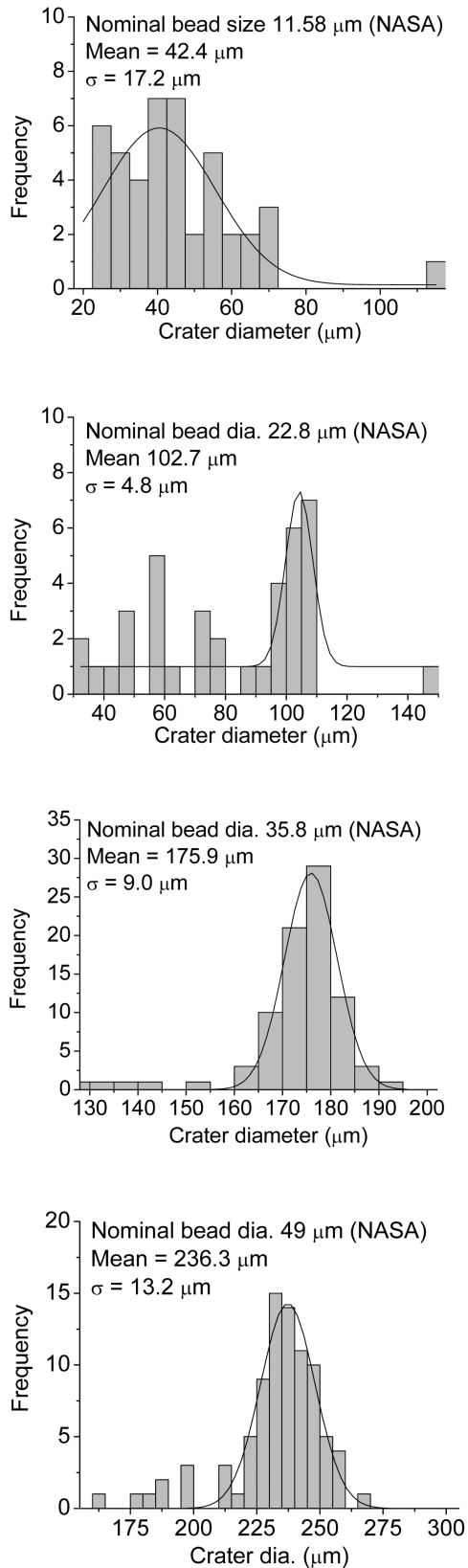


Fig. 12. Histograms of impact crater diameters for each wrapped foil shot at NASA.

6.22 km s^{-1} , see Table 1) appears to have had little systematic effect upon crater dimensions, again in accordance with the empirical equations of Humes (1991), with the velocity dependent exponent likely to give crater size dispersion of less than 3% relative.

The full line equation plotted on Fig. 13 shows an excellent linear fit to the data, with minor associated errors. The intercept on the Y-axis is very close to zero (0.68 μm), well within the stated standard deviation error ($\pm 5.04 \text{ μm}$). It can therefore be assumed to be a statistical phenomenon, rather than a true positive intercept. Although the relationship of crater size to particle diameter shows a constant linear trend across the measured range, we cannot exclude the possibility of a very slightly steeper line gradient for the very smallest particle sizes. We intend to attempt buckshot firings of particles between 1 and 10 μm in diameter to further constrain this size interval, but experimental simulation of these smallest impacts is difficult. If the fit is forced to the origin, the line gradient becomes 4.63 (an increase of about 0.01), which we recommend as the value for use in interpretation of Stardust craters.

We therefore consider that the most appropriate calibration equation for craters created by impacts onto 100 micron Al 1100 foil at around 6.1 km s^{-1} by particles between 10 μm and 80 μm in diameter and with the density of soda-lime glass is:

$$\text{Impacting particle diameter} = \frac{\text{impact crater lip diameter (D)}}{4.63} \quad (1)$$

The definition of crater size shown in Fig. 10, and as used in Equation 1, was chosen as ideal for use with scanning electron microscopy. However, other definitions of crater diameter have been employed in other studies, such as the internal diameter of the crater cavity as measured in the original surface plane of the target (e.g., Love et al. 1995), usually determined by optical microscopy. For the target foils impacted at the University of Kent, between ten and twenty craters per foil were measured using a stereo microscope. The foils were mounted on a mechanical stage and the lateral displacement was measured as the craters were moved across the field of view, with gauges accurate to $\pm 3 \text{ μm}$, although the visual acuity of the observer was probably more of the order of 5 to 10 μm . Two orthogonal internal diameters were measured per crater and were averaged. The average diameter of all the craters on each foil is given in Table 2, along with the standard deviation of each sample about the mean. No significant difference in diameter was observed between foils tightly wrapped against a supporting plate and those with free rear surfaces, even where full penetration had occurred.

The results for the measured internal crater cavity diameters versus bead diameter are shown in Fig. 14. A linear fit to the data from foils tightly wrapped against a supporting plate has been included (shown on the figure). There is a slight Y-axis offset from the origin in the fit curve intercept, but this is less dispersion than 2σ . As no data were taken for

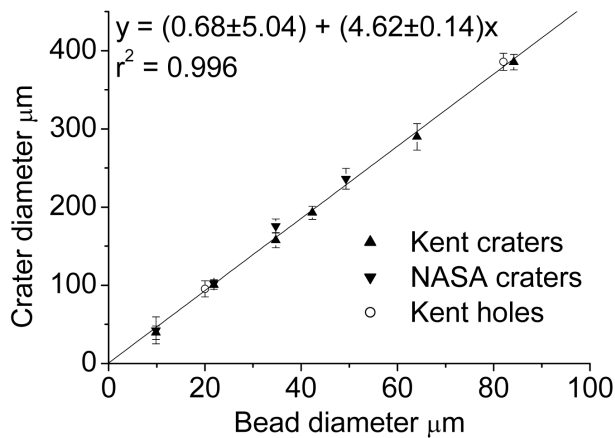


Fig. 13. Plots of average impact crater diameter against projectile average diameter: for all craters greater than four times the projectile average diameter (except the data point for the smallest projectiles).

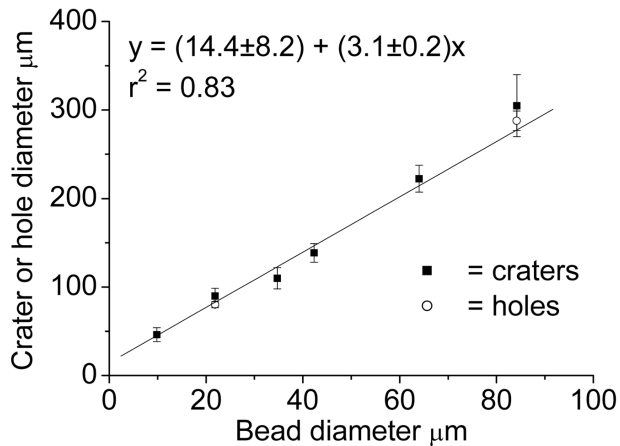


Fig. 14. Crater internal cavity diameter in the original plane of the target surface. The fit is to the crater data (squares) only, but full penetration hole data (circles) are very similar.

projectiles of less than 10 μm in diameter, and given the estimated precision, this may set the lower limit on applicability of this optical method of calibration. If we compare to the crater lip calibration (Fig. 13), the slope is reduced from 4.62 ± 0.14 to 3.1 ± 0.2 . This implies a rather smaller crater diameter as a result of the change in crater definition (to be expected), with a ratio between the two calibrations of 1.49 ± 0.1 . A variety of other definitions of crater diameter are also possible based on the sloping walls of the crater as they rise from the plane of the original undisturbed target surface to the top of the crater lips; for each the slope of the relevant calibration curve will lie between the two cases given here.

DISCUSSION AND FUTURE WORK

There are a number of potential sources of error in this calibration study which require discussion.

Table 2. Diameter of internal crater cavity measured in the original surface plane of the target by optical microscopy and compared to SEM measurement of bead diameter. All shots performed on the light gas gun at the University of Kent at Canterbury.

Measured bead diameter (μm)	Crater diameter \pm (μm)	Description
9.84	46.1 ± 7.8	Foil tight against supporting plate
21.87	89.8 ± 8.8	Foil tight against supporting plate
34.72	109.8 ± 12.0	Foil tight against supporting plate
42.3	138.5 ± 10.5	Foil tight against supporting plate
64.05	222.3 ± 15.2	Foil tight against supporting plate
84.18	304.8 ± 35	Foil tight against supporting plate
21.87	80.1 ± 3.4	Foil with free rear surface
84.18	287.8 ± 11	Foil with free rear surface

The complexity of electron image tone distribution is not suited to automated image processing and appropriate placement of calipers on stored digital images has to be performed manually. In the reported study, all of the electron imagery and measurement was performed by one person (ATK), and all of the optical measurements by one person (MJB) and hence perception of the correct features may be considered consistent throughout each data set. Images with a relatively low number of pixels spanning the feature of interest (e.g., small craters or spheres) inevitably compromise measurement precision, although repeated measurements from the same crater do yield reproducible location of points, and the range of individual measurements for the three diameters is small, typically less than 5% dispersion between the crater maximum and minimum diameter average (see final column of Table 1).

Incomplete edge “turnover” and detachment of extensive segments of the rim was observed in some craters, limiting the number of diameter measurements that could be made reliably. However, careful handling of the foils ensured that no surface flattening occurred, as this might depress the curved portion of the crater lip and thereby change the apparent crater diameter measurement. The handling of impacted soft aluminum foils during sample extraction from the Stardust aerogel collector may also generate a suite of crater dimension modifications due to localized shortening during bending to produce an approximately planar sheet, and craters in these regions of the foil should be examined with care. Although the majority of crater rims approximated a circular plan outline in backscattered electron images with beam normal incidence, secondary electron imagery did sometimes reveal more complex subsurface morphology. A few craters (31/433 craters with three diameters measured) display oval rim outlines, defined herein as maximum/

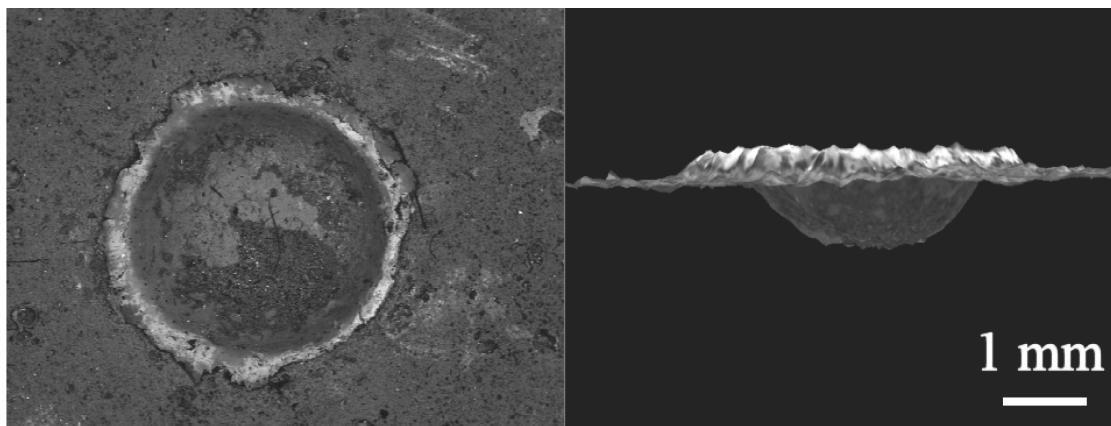


Fig. 15. A backscattered electron image of an impact crater on titanium metal (left) and projection of a three-dimensional digital model derived from tilted inclination images of the same crater (right). It is possible to measure both crater depth below and crater inner diameter at the ambient target surface. Reconstruction using MEX software, courtesy of Alicona Imaging GmbH.

minimum diameter exceeding 1.10, but none exceeded 1.19. Deviations from perfect circularity may have complex sources that are difficult to track down, but may include non-spherical impactors, spheres with protuberances and spheres containing bubbles (all observed in the optical microscope), as well as variation in the size and orientation of target crystals and impact proximity to associated grain boundaries.

The “blank” shot at Kent, using an empty sabot, demonstrated that the light gas gun itself yields only a small number of impacts from mobilized gun components (such as the burst disk, high pressure piston or sabot) generating craters of a size comparable to those from the smallest glass bead projectiles (only 11 craters of 30–50 μm in diameter on the entire foil). Although there are numerous craters of less than 20 μm in diameter, we suggest that there is no significant contribution from mobilized parts of the apparatus to the numbers of craters in our calibration plot.

Comparison of craters from tightly-wrapped foil to those on foils with a rear free surface shows that variation in the proximity of the foil to the underlying frame will have a minor effect. Two shots, with 21.87 and 84.14 micron determined particle diameters, were taken with free rear surface targets. In both cases the craters showed a minor reduction in average crater lip diameter when compared to the calibration line for craters from shots with tightly wrapped foil, but with the standard deviation still overlapping the linear fit to the entire data set. As these were “worst-case” situations, with no physical coupling to the underlying aluminum frame, we consider that variation in the tightness of foil wrapping will not seriously compromise application of our calibration data to the Stardust spacecraft.

Comparability of Projectiles to Micrometeoroid Materials

In this paper, we have shown that there is a simple relationship between impacting particle diameter and the width of the crater produced on Stardust foils (impacting

particle diameter = impact crater diameter/4.62). What factors might cause cometary particle impacts to deviate from this simple scale relationship?

Experimental measurements of aluminum target crater formation under closely controlled conditions reported in previous studies (e.g., Cour-Palais 1987) have shown that crater dimensions such as depth are dependent upon particle mass, density, velocity, and impact incidence angle (but see below). For instance, Humes (1991):

$$\begin{aligned} \text{Crater depth below ambient surface} = \\ 0.42 * (\text{particle mass}^{0.352}) * (\text{particle density}^{0.166}) * \\ (\text{particle velocity}^{0.666}) * \\ (\cosine \text{ of incidence angle}^{0.666}) \end{aligned} \quad (2)$$

Our experiments used spherical glass projectiles of 2.4 g cm^{-3} density, similar but somewhat greater than that determined for cometary dust particles (c. 2.0 g cm^{-3} , Love et al. 1994; 1.6 to 2.4 g cm^{-3} , McDonnell and Gardner 1999), but less than that determined by Burchell et al. (1998) for particles impacting spacecraft in LEO (3.4 g cm^{-3}). However, the small value of the density exponent in the equation above suggests that crater dimension should be relatively insensitive to density differences between glass and silicate micrometeoroid particles. Although the mineral composition and fine structure is as yet unknown from pristine samples collected in space, there is extensive literature on both remote sensing of cometary dust by infrared spectrophotometry (e.g., Wooden et al. 1999) and the composition and structure of delicate interplanetary dust particles captured in the stratosphere (see review by Rietmeijer 1998). Both suggest that many dust particles will contain porous aggregates of small grains of silicates including the pyroxene enstatite ($\rho = 3.2 \text{ g cm}^{-3}$) and forsterite olivine ($\rho = 3.2 \text{ g cm}^{-3}$) as well as iron sulfides ($\rho = 4.6 \text{ g cm}^{-3}$), amorphous silicates, and organic matter of density around 1 g cm^{-3} . Although it is important to utilize projectiles that will produce similar impact effects to those expected to be generated by cometary

particles, it is not possible to simulate these fragile aggregates, and we await examination of the returned foils to determine whether shallow, broad, and irregular impact features may indicate very low density and complex grain impacts. Nevertheless, we have performed impact experiments with enstatite and olivine, among other minerals, and have begun initial analysis of the role of inequant particle shape on crater dimensions.

Love et al. (1995) demonstrated that there is relatively little variation in the ratio of crater depth to diameter in micrometeoroid impact craters of a wide range of sizes upon LDEF space-facing substrates. It is therefore reasonable to assume that for silicate-dominated particles there is a similar crater diameter relationship to impacting particle parameters. However, Wallis et al. (2002) demonstrated that for impacts onto aluminum, by mineral grains at a speed of 5.3 km s^{-1} , there may be substantial variation in the shape of impact features as a function of particle characteristics, especially density and hardness, and that depth may no longer be at a constant ratio to crater diameter. Hörz et al. 1993 have shown that laboratory impact experiments can yield important projectile size calibration data for aluminum foils, but to date, no extensive calibration of crater shape dependence upon particle physical properties has been published for impacts onto substrates akin to the Stardust foils by particles analogous to cometary minerals.

To address this issue, five other foil shots were also performed at Kent using projectiles of: 1) crushed Orgueil C1 carbonaceous chondrite meteorite; 2) a mixture of olivine (38–53 μm by sieving) and Al_2O_3 grains (typically 3 μm); 3) pyroxene (enstatite) less than 38 μm (sieved); 4) crushed basalt glass from an analytical test sample from the United States Geological Survey, and 5) a mixture of enstatite, olivine, diopside, anorthite, pyrrhotite, magnetite, calcite, Orgueil fragments, and 22 micron soda-lime glass spheres. These provided analogue samples for compositional analysis of impact residues under a range of original projectile size, shape, chemical composition, density, hardness, etc., and will be described in a future publication. Accurate three-dimensional crater-shape determination is a difficult and time-consuming process, although modern stereometry routines such as MEX, marketed by Alicona, may allow precise feature measurement (e.g., Fig. 15), including determination of crater profile, depth, and width at the plane of the ambient foil surface.

CONCLUSION

A robust calibration for impactor size versus impact crater size has been obtained for the aerogel mounting foils carried by the Stardust return capsule. This covers a wide size range of interest (impactor sizes ~ 10 to $85 \mu\text{m}$). Extrapolation of the size calibration presented in this paper to a projectile diameter of 1 micron is probably acceptable, but for smaller

sizes it may be necessary to use other types of accelerators and projectiles (e.g., Goldsworthy et al. 2003) and simulations of impact for nanometer-scale particles (e.g., using numerical molecular dynamics such as the SPaSM code of Beasley and Lomdahl 1994). For particles larger than $100 \mu\text{m}$ in diameter, it is important to note the potential role of the discontinuity at the rear of the foil and possible poor mechanical coupling with the underlying Al 6061 frame. Should craters of greater than $400 \mu\text{m}$ in diameter be observed on Stardust foils, it may be helpful to perform more shots, with larger projectiles than were used in this study. In conclusion, a reasonably reliable and independent estimate of the impactor size flux can be obtained from the observed crater size distribution on the Stardust foils.

Acknowledgments—We thank the Natural History Museum London for access to electron microscope facilities and Nick Foster (University of Kent) for information on glass sphere projectile fragmentation from impacts onto silica aerogel. The JSC experiments were supported by the Stardust project funds.

Editorial Handling—Dr. Donald Brownlee

REFERENCES

- Beasley D. M. and Lomdahl P. S. 1994. Message-passing multi-cell molecular dynamics on the Connection Machine 5. *Parallel Computing* 20:173–195.
- Bernhard R. P. and Hörz F. 1995. Craters in aluminium 1100 by soda-lime glass spheres at 1 to 7 km/s. *International Journal of Impact Engineering* 17:69–80.
- Bernhard R. P., Durin C., and Zolensky M. E. 1994a. Scanning electron microscope/energy dispersive X-ray analysis of impact residues in LDEF tray clamps. In *LDEF—69 months in space*, edited by Levine A. S. Part 2. NASA Conference Publication #3194. Washington, D.C.: National Aeronautics and Space Administration. pp. 541–549.
- Bernhard R. P., See T. H., and Hörz F. 1994b. Projectile compositions and modal frequencies on the “Chemistry of Micrometeoroids” LDEF experiment. In *LDEF—69 months in space*, edited by Levine A. S. Part 2. NASA Conference Publication #3194. Washington, D.C.: National Aeronautics and Space Administration. pp. 551–573.
- Brownlee D. E., Joswiak D., Bradley J.P., and Hörz, F. 1994. Interplanetary meteoroid debris in LDEF metal craters. In *LDEF—69 months in space*, edited by Levine A. S. Part 2. NASA Conference Publication #3194. Washington, D.C.: National Aeronautics and Space Administration. pp. 577–584.
- Brownlee D. E., Tsou P., Anderson J. D., Hanner M. S., Newburn R. L., Sekanina Z., Clark B. C., Hörz F., Zolensky M. E., Kissel J., McDonnell J. A. M., Sandford S. A., and Tuzzolino A. J. 2003. Stardust: Comet and interstellar dust sample return mission. *Journal of Geophysical Research* 108(E10):8111, doi:10.1029/2003JE002087.
- Burchell M. J. and MacKay N. 1998. Crater ellipticity in hypervelocity impact on metals. *Journal of Geophysical Research* 103:22761–22774.
- Burchell M. J., Cole M. J., McDonnell J. A. M., and Zarnecki J. C. 1999. Hypervelocity impact studies using the 2 MV Van de

- Graaff dust accelerator and a two-stage light gas gun of the University of Kent at Canterbury. *Measurement Science and Technology* 10:41–50.
- Christiansen E., Cykowski E., and Ortega J. 1993. Highly oblique impacts into thick and thin targets. *International Journal of Impact Engineering* 14:157–168.
- Cour-Palais B. G. 1987. Hypervelocity impacts in metals, glass and composites. *International Journal of Impact Engineering* 5: 681–692.
- Davis J. R. 1998. *Metals handbook. Desk edition*, 2nd ed. Materials Park, Ohio: ASM International.
- Dunn B. D. 1997. *Metallurgical assessment of spacecraft parts, materials and processes*, 2nd ed. Chichester, West Sussex: John Wiley and Sons.
- Goldsworthy B. J., Burchell M. J., Cole M. J., Armes S. P., Khan M. A., Lascelles S. F., Green S. F., McDonnell J. A. M., Srama R., and Bigger S. W. 2003. Time of flight mass spectrometry of ions in plasmas produced by hypervelocity impacts of organic and mineralogical microparticles on a Cosmic Dust Analyser. *Astronomy & Astrophysics* 409:1151–1167.
- Graham G. A., Kearsley A. T., Wright I. P., Grady M. M., Drolshagen G., McBride N. M., Green S. F., Burchell M. J., Yano H., and Elliott R. 2001. Analysis of impact residues on spacecraft surfaces: possibilities and problems. In *Proceedings of the 3rd European Conference on Space Debris*, edited by Sawaya-Lacoste H. ESA Special Publication #473. Noordwijk: ESA Publications Division, ESTEC. pp.197–203.
- Graham G. A., Kearsley A. T., Drolshagen G., McDonnell J. A. M., Wright I. P., and Grady M. M. 2004. Mineralogy and microanalysis in the determination of cause of impact damage to spacecraft surfaces. In *Forensic geoscience: Principles, techniques and application*, edited by Pye K. and Croft D. J. Special Publication #232. London: The Geological Society of London. pp. 137–146.
- Graham G. A., Sheffield-Parker J., Bradley J. P., Kearsley A. T., Dai Z. R., Mayo S. C., Teslic N., Snead C., Westphal A. J., Grant P. A., and Ishii H. A. 2005. Electron beam analysis of micrometeoroids captured in aerogel as Stardust analogues (abstract #2078). 36th Lunar and Planetary Science Conference. CD-ROM.
- Grün E., Fechtig H., Giese R. H., Kissel J., Lindblad B.-A., Linkert D., Maas D., McDonnell J. A. M., Morfill G. E., Schwehm G., and Zook H. A. 1992. The Ulysses dust experiment. *Astronomy and Astrophysics Supplement Series* 92:411–423.
- Grün E., Baguhl M., Divine N., Fechtig H., Hamilton D. P., Hanner M. S., Kissel J., Lindblad B.-A., Linkert D., Linkert G., Mann I., McDonnell J. A. M., Morfill G. E., Polansky C., Riemann R., Schwehm G., Siddique N., Staubach P. and Zook H. A. 1995. Three years of Galileo dust data. *Planetary and Space Science Review* 43:953–969.
- Hörz F., Cintala M., Bernhard R. P. and See T. H. 1993. Dimensionally scaled penetration experiments to extract projectile sizes from space exposed surfaces. *International Journal of Impact Engineering* 14: 347–358.
- Hörz F., Zolensky M. E., Bernhard R. P., See T. H., and Warren J. L. 2000. Impact features and projectile residues in aerogel exposed on Mir. *Icarus* 147:559–579.
- Humes D. H. 1991. Large craters on the meteoroid and space debris impact experiment. In *LDEF—69 months in space*, edited by Levine A. S. Part 1. NASA Conference Publication #3134. Washington, D.C.: National Aeronautics and Space Administration. pp. 399–418.
- Kearsley A. T., Drolshagen G., McDonnell J. A. M., Mandeville J.-C., and Moussi A. 2005. Impacts on Hubble Space Telescope solar arrays: Discrimination between natural and manmade particles. *Advances in Space Research* 35:1254–1262.
- Kissel J., Glasmachers A., Grün E., Henkel H., Höfner H., Haerendel G., von Hoerner H., Jessberger E. K., Krueger F. R., Möhlmann D., Greenberg J. M., Langevin Y., Silén J., Brownlee D., Clark B. C., Hanner M. S., Hörz F., Sandford S., Sekanina Z., Tsou P., Utterback N. G., Zolensky M. E., and Heiss C. 2003. Cometary and Interstellar Dust Analyzer for comet Wild-2, *Journal of Geophysical Research* 108(E10): 8114, doi:10.1029/2003JE002091.
- Love S. G., Brownlee D. E., King N. L., and Hörz F. 1995. Morphology of meteoroid and debris impact craters formed in soft metal targets on the LDEF satellite. *International Journal of Impact Engineering* 16:405–18.
- Love S.G., Joswiak D. J., and Brownlee D. E. 1994. Densities of stratospheric micrometeorites. *Icarus* 111:227–236.
- McDonnell J. A. M. and Gardner D. J. 1998. Meteoroid morphology and densities: Decoding satellite impact data. *Icarus* 133:25–35.
- Moussi A., Drolshagen G., McDonnell J. A. M., Mandeville J.-C., Kearsley A. T., and Ludwig H. 2005. Hypervelocity impacts on HST solar arrays and the debris population. *Advances in Space Research* 35:1243–1253.
- Rietmeijer F. J. M. 1998. Interplanetary dust particles. In *Planetary materials*, edited by Papike J. J. Reviews in Mineralogy and Geochemistry, vol. 36. Washington, D.C.: Mineralogical Society of America. pp. 1–95.
- See T. H., Mack K. S., Warren J. L., Zolensky M. E. and Zook H. A. 1994. Continued investigation of LDEF's structural frame and thermal blankets by the meteoroid and debris special investigation group. In *LDEF—69 months in space*, edited by Levine A. S. Part 2. NASA Conference Publication #3194. Washington, D.C.: National Aeronautics and Space Administration. pp. 313–324.
- Tsou P., Brownlee D. E., Sandford S. A., Hörz F., and Zolensky M. E. 2003. Wild-2 and interstellar sample collection and Earth return. *Journal of Geophysical Research* 108 (E10):8113, doi:10.1029/2003JE002109.
- Tuzzolino A. J., Economou T. E., Clark B. C., Tsou P., Brownlee D. E., Green S. F., McDonnell J. A. M., and Colwell M. T. S. H. 2004. Dust measurements in the coma of comet 81P/Wild-2 by the Dust Flux Monitor Instrument. *Science* 304:1776–1780.
- Wallis D., Solomon C. J., Kearsley A. T., Graham G., and McBride N. M. 2002. Modelling radially symmetric impact craters with Zernike polynomials. *International Journal of Impact Engineering* 27:433–457.
- Warren J. L., Zook H. A., Allton J. H., Clanton U. S., Dardano C. B., Holder R. R., Marlow R. A., Schultz R. H., Watts L. A., and Wentworth S. J. 1989. The detection and observation of meteoroid and space debris impact features on the solar Max satellite. Proceedings, 19th Lunar and Planetary Science Conference. pp. 641–657.
- Wooden D. H., Harker D. E., Woodward C. E., Butner H. M., Koike C., Witteborn F. C., and McMurtry C. W. 1999. Silicate mineralogy of the dust in the inner coma of comet C/1995 01 (Hale-Bopp) pre and post-perihelion. *The Astrophysical Journal* 517:1034–1058.
- Zolensky M. E., Zook H. A., Hörz F., Atkinson D. R., Coombs C. R., Watts A. J., Dardano C. B., See T., Simon C. G., and Konard W. H. 1994. Interim report of the meteoroid and debris special investigation group. In *LDEF—69 months in space*, edited by Levine A. S. Part 2. NASA Conference Publication #3194. Washington, D.C.: National Aeronautics and Space Administration. pp. 277–302.